An Efficient Polarimetric Persistent Scatterer Interferometry Algorithm for Dual-Pol Sentinel-1 Data

Feng Zhao, *Member, IEEE*, Leixin Zhang, Teng Wang, Yuxuan Zhang, Shiyong Yan, and Yunjia Wang

***Abstract*—With time-series PolSAR images, polarimetric persistent scatterer interferometry (PolPSI) algorithms can obtain optimized interferograms with overall better phase quality than any single-pol channel for ground deformation monitoring. Moreover, the open access of Sentinel-1 PolSAR data makes it possible for applications of PolPSI over large regions worldwide. However, the optimum scattering mechanism usually has to be searched in a high dimension solution space by PolPSI techniques from each pixel. This is with very high or even unacceptable computational costs if satisfactory results are expected. To this end, an efficient and effective PolPSI algorithm named as TP-ESM is proposed with Sentinel-1 data in this study, which optimizes pixels' interferograms by a weighted sum of their corresponding VV and VH channel interferograms. The effectiveness of TP-ESM is tested together with two other PolPSI techniques [i.e., TP-MSM and exhaustive search polarimetric optimization (ESPO)] over Beijing with 46 Sentinel-1 PolSAR images. The results show that TP-ESM can obtain similar optimized interferometric phases with ESPO over high quality pixels, and the ground deformation monitoring pixel density improvement achieved by TP-ESM and ESPO w.r.t. conventional PSI approach (with VV data) is 35% and 43%, respectively. On the other hand, the TP-MSM approach is found not applicable to Sentinel-1 data. Considering the negligible computational cost of TP-ESM w.r.t. ESPO, it presents a quite good performance on both interferograms' optimizations and ground deformation monitoring. Moreover, the proposed TP-ESM outperforms ESPO on distributed scatterers pxiels' optimization, and it is anticipated to have promising performances on other PolSAR images acquired by other sensors.**

Manuscript received 26 April 2022; revised 8 July 2022, 27 September 2022, and 15 January 2023; accepted 20 March 2023. Date of publication 23 March 2023; date of current version 7 April 2023. This work was supported in part by the National Natural Science Foundation of China under Grant 42004011, in part by the National Key R&D Program of China under Grant 2022YFE0102600, in part by the China Postdoctoral Science Foundation under Grant 2020M671646, in part by the Open Research Fund of Jiangsu Key Laboratory of Resources and Environmental Information Engineering, CUMT under Grant JS202105, and in part by the Priority Academic Program Development (PAPD) of Jiangsu Higher Education Institutions (Science and Technology of Surveying and Mapping). *(Corresponding author: Yunjia Wang.)*

Feng Zhao is with the Jiangsu Key Laboratory of Resources and Environmental Information Engineering, China University of Mining and Technology, Xuzhou 221116, China, and also with the School of Environment Science and Spatial Informatics, China University of Mining and Technology, Xuzhou 221116, China (e-mail: feng.zhao@cumt.edu.cn).

Leixin Zhang, Teng Wang, Yuxuan Zhang, Shiyong Yan, and Yunjia Wang are with the Key Laboratory of Land Environment and Disaster Monitoring, MNR, China University of Mining and Technology, Xuzhou 221116, China, and also with the School of Environment Science and Spatial Informatics, China University of Mining and Technology, Xuzhou 221116, China (e-mail: zhangleix1028@cumt.edu.cn; wteng611@cumt.edu.cn; zhangyx99@cumt.edu.cn; yanshiyong@cumt.edu.cn; wyj4139@cumt.edu.cn).

Digital Object Identifier 10.1109/JSTARS.2023.3260850

***Index Terms*—Ground deformation monitoring, interferometric phase optimization, persistent scatterer interferometry (PSI), polarimetry, sentinel-1 PolSAR images.**

I. Introduction

DIFFERENTIAL synthetic aperture radar (SAR) interferometry (DInSAR) is an active remote sensing technique that is able to obtain ground deformation independent of weather and solar illumination conditions. It has been applied to the monitoring of earthquakes [1], volcanic explosions [2], glacier motions [3], etc. However, the performance of DInSAR is limited mainly by the spatial-temporal decorrelations [4] and the atmospheric phase screen (APS) [5]. To overcome the shortcomings of the DInSAR technique, the persistent scatterer interferometry (PSI) techniques have been proposed and developed into a routinely used tool for terrain motion monitoring in the recent two decades [6], [7], [8], [9], [10], [11]. PSI techniques eliminate the impacts of decorrelations by identifying those pixels with temporally stable phases (i.e., PS pixels) for ground deformation monitoring [7], [11], and the influence of APS can be reduced by employing APS filtering techniques [6], [11], [12] or estimation algorithms [13], [14]. Due to its high efficiency and accuracy, PSI techniques have been successfully used to monitor surface or infrastructures' displacements related with subsidence [15], [16], mining [17], earthquakes [18], volcanoes [19], landslides [20], underground coal fires [21], etc.

Despite the great success of PSI applications in a variety of areas, it is limited by the fact that it can only measure surface displacements over qualified pixels [22]. Thus, very sparse or no pixels could be employed for the traditional PSI applications in areas (f.i., suburban and vegetation areas) where distributed scatterers (DS) or noisy pixels are the majority [23]. However, geological hazards mostly occur over these areas where ground deformation monitoring is necessary. Under this circumstance, various algorithms to optimize pixels' phases have been proposed, and it has been a research hotspot during the last decade. Generally, there are two approaches to optimize pixels' phases.

On the one hand, DS pixels are supposed to have similar scattering mechanisms (SMs) with their spatial neighborhoods, and based on this the so-called DS-InSAR techniques such as the SqueeSAR [22], CAESAR [24], and their variants [25], [26] have been proposed. DS-InSAR techniques optimize pixels mainly in three steps. First, statistically homogeneous pixels

(SHPs) of each pixel are identified by algorithms such as the Kolmogorov–Smirnov (KS) test, the Anderson–Darling (AD) test, and FaSHP [27]. Then, all the pixels are usually classified into PS or DS pixels by their SHP numbers. Finally, the recognized SHPs of each DS pixel are used for the optimization of its time-series interferometric phase by employing the techniques, such as phase linking [28] and other algorithms [29], [30], [31], [32]. As the result, by reducing the phase noise of DS pixels, a part of DS pixels with medium decorrelations (f.i., pixels over bare ground) are qualified for measuring terrain displacements, such as PS pixels. Therefore, more density of pixels can be used for the ground deformation monitoring over wider regions with DS-InSAR algorithms.

On the other hand, inspired by the polarimetric SAR interferometry (PolInSAR) technique [33], some researchers proposed to optimize pixels' interferometric phases from the perspective of SAR polarimetry. As it is known that targets on the ground respond differently to electromagnetic waves with different polarizations [34]. In other words, each SAR pixel is with different phase noise levels over different polarimetric channels (f.i., HH, VV, and VH channels) that correspond with different SMs. Thus, by searching and then using the optimum polarimetric channel (i.e., SM) with the lowest decorrelations for PSI applications, more density of qualified pixels can be obtained for ground deformation monitoring [33], [34]. This category of PSI techniques that make use of time-series PolSAR images is the polarimetric PSI (PolPSI) algorithms.

Mainly due to the lack of long time-series PolSAR images, conventional PSI techniques are limited to single polarization SAR images. In 2009, with the PolSAR images obtained by a ground-based SAR sensor, the first PolPSI technique, i.e., BEST [35], has been proposed by Pipia from Universitat Politcècnica de Catalunya. With more and more sensors in orbit are capable of acquiring PolSAR images (f.i., Radarsat-2, ALOS-2, TerraSAR-X, Sentinel-1, COSMO-SkyMed-2, and LT-1), it is possible to apply PolPSI techniques on ground deformation monitoring over more regions. Meanwhile, more advanced PolPSI algorithms have been proposed with the spaceborne PolSAR images [36], [37], [38], [39], [40], [41], [42], [43], [44], [45], [46], [47], [48].

Conventionally, PolPSI techniques perform pixels' polarimetric optimization with interferometric phase quality metrics, and accordingly they can be classified into mainly three categories [49]. These three category PolPSI techniques are PolPSI-ADI (with the amplitude dispersion index as the phase quality metric, better for PS pixels' optimization) [36], [46], [50], PolPSI-COH (with the coherence as the phase quality metric, better for DS pixels' optimization) [35], [37], [41], [46] and PolPSI-AOS (with adaptive optimization strategies) [39], [43], [45]. Nevertheless, based on 13 ALOS-2 full-polarization SAR images, a PolPSI technique that without any phase quality metric has been proposed recently [48]. This new PolPSI technique carries out the polarimetric optimization by constructing the total power (TP) interferograms, thus, it is named as TP-MSM in this study [48].

In essence, TP-MSM optimizes pixels' interferometric phases by a weighted sum of all the interferograms over the three Pauli channels, where the weights of each Pauli channel of a pixel is determined by its interferogram amplitude [48]. The TP-MSM method is very efficient since it requires no searching for the optimum SM for each pixel as the exhaustive search polarimetric optimization (ESPO) method that is considered with the best optimization effect. More importantly, it is reported to have a better performance than the ESPO method (with D_A phase quality index) on the employed 13 ALOS-2 full-polarization SAR images [48]. Nevertheless, to the authors' best knowledge, the extraordinary performance of TP-MSM with other PolSAR datasets has not yet been verified and published. It could have problems when the interferogram amplitudes are seriously affected by the speckle noise or with lower resolutions PolSAR images [51]. Moreover, it may introduce artificial interferometric phases in interferograms as different SMs (i.e., different weights) are used for different interferograms. Therefore, the effectiveness of TP-MSM on different PolSAR images (acquired by different SAR sensors with different wavelengths and resolutions) over different areas needs to be further investigated and verified.

Benefiting from the open access policy of the Copernicus project of the European Space Agency (ESA), a huge amount of Sentinel-1 double polarimetric (DP) SAR images worldwide can be easily obtained by users, frequently. Recently, a few studies [49], [52], [53] that apply PolPSI algorithms on the Sentinel-1 PolSAR images have been reported. However, most of the existing PSI applications only use VV channel Sentinel-1 SAR images. This is caused mainly by two reasons. On the one hand, if satisfactory results are expected to be obtained by PolPSI techniques, it is necessary to employ the ESPO method for the polarimetric optimization with Sentinel-1 DP images. This is unacceptable for large regions' applications as very long optimization times are required. On the other hand, due to the lack of one polarimetric channel information and the medium spatial resolution, even if ESPO is performed, the improvement on final ground deformation results could be limited over some areas. As the polarimetric configuration and pixels' resolution are fixed, thus, the only possible approach to make PolPSI with Sentinel-1 data cost-effective is to develop efficient PolPSI techniques.

To this end, inspired by TP-MSM [48], a new efficient PolPSI algorithm is proposed with DP Sentinel-1 data in this study. In addition, TP-MSM is first tested on the Sentinel-1 images. The main novelty of this article is twofold. First of all, a new efficient PolPSI technique named as TP-ESM is proposed, which applies the equal scattering mechanism (ESM) constraint [54] and presents a quite promising performance. Second, the TP-MSM method is tested on the Sentinel-1 data, and as the results show that it is not applicable to the DP Sentinel-1 data.

The rest of this article is organized as follows. The PolPSI basis, the ESPO with D_A, TP-MSM, and the proposed TP-ESM are introduced in Section II. Section III gives out the test area and data. In Section IV, interferograms' polarimetric optimization results and ground deformation time-series results obtained by employed approaches are presented and compared. Finally, discussions are made in Section V. Finally, Section VI concludes this article.

II. Methods

PolPSI algorithms mainly consist of two procedures, i.e., the polarimetric optimizations of interferograms and the PSI processing. Based on the generated interferograms (i.e., the VV channel interferograms or optimized ones), the StaMPS algorithm is used for the PSI processing in this study for each approach. Details of retrieving time-series deformation by StaMPS can be found in [11] and [12]. As the polarimetric optimization of interferograms is the focus and core of PolPSI techniques, it will be detailed in this section.

A. PolInSAR With DP Sentinel-1 Data

The scattering matrix of one DP Sentinel-1 SAR image can be expressed as

$$S = \begin{bmatrix} 0 & S_{\text{vh}} \\ S_{\text{vh}} & S_{\text{vv}} \end{bmatrix} \tag{1}$$

where S_{vv} and S_{vh} are the vertical copolar (i.e., VV) and the cross-polar channel (i.e., VH) corresponding element, respectively. Under the Pauli basis, the scattering vector related to the scattering matrix is defined as

$$k = [S_{\text{vv}},\ 2S_{\text{vh}}]^T. \tag{2}$$

Two PolSAR images acquired at different locations are required for PolInSAR, and the corresponding PolInSAR vector constructed by these two PolSAR images can be expressed as

$$K = [k_1,\ k_2]^T \tag{3}$$

where k_1 and k_2 are the scattering vector defined by (2) for the first and second PolSAR image, respectively [33], [34]. It can be found from (2) and (3) that two interferograms can be generated from the two polarimetric channels, respectively. Therefore, to obtain one optimized interferogram by the two polarimetric channels, two normalized complex projection vectors ω_1 and ω_2 are introduced in PolInSAR. These two normalized complex projection vectors are usually regarded as SMs, and they are given as

$$\boldsymbol{\omega}_{1,2} = \begin{bmatrix} \cos(\alpha) \\ \sin(\alpha)e^{j\psi} \end{bmatrix}, \quad \begin{cases} 0 \le \alpha \le \pi/2 \\ -\pi \le \psi < \pi \end{cases} \tag{4}$$

where α and ψ are two parameters that determine the SM and phase relation of the scatterer (i.e., pixel), respectively [33], [34], [49], [52]. Then, by, respectively, projecting k_1 and k_2 into the two SMs (i.e., ω_1 and ω_2), two complex scattering coefficients μ_1 and μ_2 can be obtained as

$$\mu_i = {\omega_i}^{\dagger} \cdot k_i, \quad i = 1, 2 \tag{5}$$

where $\dagger$ is the conjugate transpose. μ_1 and μ_2 are similar to master and slave single-look complex (SLC) images for the single-pol SAR data case. Thus, one interferogram can be generated with the obtained μ_1 and μ_2 as

$$I = \mu_1 \cdot {\mu_2}^{\dagger} = ({\omega_1}^{\dagger} \cdot k_1) \cdot ({\omega_2}^{\dagger} \cdot k_2)^{\dagger} \tag{6}$$

where I is the two PolSAR images synthesized interferogram [33], [34].

The polarimetric optimization of the PolInSAR technique is to find the optimum ω_1 and ω_2 that make the synthesized interferogram I with the best interferometric phase quality. For PSI applications, to avoid introducing artificial changes in scatters' phase center along time, which could be misinterpreted as scatters' deformations, the ESM [54] constraint is usually applied. In other words, for one pixel, its corresponding optimum ω for the optimization is forced to be identical for all the PolSAR images along time. Under this circumstance, the polarimetric optimization of PolPSI is to search for each pixel its best SM (i.e., ω) along time. This optimum SM corresponds with the overall lowest decorrelations over all the generated interferograms for the optimizing pixel. Different optimization algorithms have been developed, among which the ESPO method [38] is considered with the best optimization performance.

B. Interferometric Phase Optimization With the ESPO Method

To carry out the polarimetric optimization for PolPSI by employing the ESPO method, one phase quality metric should be first selected. Among the available phase quality metrics for ESPO, the dispersion of amplitude (i.e., D_A) is mostly employed to optimize full-resolution interferograms (or for PS candidates). D_A in the polarimetric case can be expressed as

$$D_A = \frac{\sigma_A}{m_A} = \frac{1}{\overline{|\omega^{\dagger}k|}} \sqrt{\frac{1}{N}\sum_{i=1}^{N}\left(|\omega^{\dagger}k_i| - \overline{|\omega^{\dagger}k|}\right)^2} \tag{7}$$

with

$$\overline{|\omega^{\dagger}k|} = \frac{1}{N}\sum_{i=1}^{N}|\omega^{\dagger}k_i| \tag{8}$$

where σ_A and m_A are the standard deviation and mean of the amplitudes of synthesized SAR images [obtained by (5)], the overline indicates the empirical mean value, N is the number of images, and k_i represents the scattering vector of the ith PolSAR image [38], [41].

Based on D_A, one by one, all the pixels over interferograms are optimized by ESPO. Specifically, the ESPO method optimizes every pixel by exhaustive searching for the optimum α and ψ values that minimize its D_A [calculated by (7) and (8)] through all possible α and ψ solutions. Then, by the obtained optimum α and ψ values for each pixel, the polarimetric optimized interferograms can be generated according to (4)–(6).

C. Interferometric Phase Optimization With the PolInSAR TP Method

A PolPSI technique based on the PolInSAR TP method has been proposed and tested with 13 ALOS-2 quad-pol SAR images in [48], where the ESM constraint does not apply. Thus, the multi SMs strategy applies to this PolPSI technique, and it is named as TP-MSM [48] in this article. On the contrary, by applying the ESM constraint, a new PolPSI algorithm based on the construction of TP interferograms is proposed in this study. We name the new PolPSI technique as the TP-ESM method. The interferograms' optimization methods of the two PolPSI methods are introduced in this section.

1) Interferometric Phase Optimization With TP-MSM Method: Given a pair of PolSAR images, one optimized interferogram employing TP-MSM can be obtained by [48]

$$I_{\text{TP-MSM}} = \left|S_{\text{vv},1} \cdot S_{\text{vv},2}^{\dagger}\right| \cdot e^{i\phi_{\text{vv}}} + \left|4 \cdot S_{\text{vh},1} \cdot S_{\text{vh},2}^{\dagger}\right| \cdot e^{i\phi_{\text{vh}}} \quad (9)$$

where $I_{\text{TP-MSM}}$ is TP-MSM optimized interferogram, $\dagger$ refers to the conjugate transpose, ϕ_{vv} and ϕ_{vh} are the interferometric phase of VV and VH channel, respectively. $S_{\text{vv},1}$ and $S_{\text{vv},2}$ in (9) represent the VV channel SAR images of the first and second PolSAR images forming the interferogram, respectively. Likewise, $S_{\text{vh},1}$ and $S_{\text{vh},2}$ are the VH channel SAR images of the first and second PolSAR images, respectively [48].

It can be observed from (9) that the optimized interferogram is actually the weighted sum of the VV and VH channel interferograms, and the two weights are determined by the TP of the two corresponding polarimetric channels. Therefore, pixels' phase centers over the optimized interferogram are mainly determined by the stronger SMs between the two available polarimetric channels, which are supposed to with lower decorrelations and better phase qualities [48].

The TP-MSM method optimizes each interferogram separately, and it does not employ the ESM constraint. Thus, the phase center of each pixel could change from one interferogram to the other as pixels amplitudes (determine the weight of each polarimetric channel) could change over time. In other words, for one particular pixel, TP-MSM introduces different (multiple) SMs to optimize it over each interferogram.

2) Interferometric Phase Optimization With TP-ESM Method: A new PolPSI method (i.e., TP-ESM) is proposed to optimize interferograms in this study. Different from the TP-MSM method, TP-ESM applies the ESM constraint on the optimization. In other words, each pixel is optimized with an identical SM over all the interferograms, which can avoid introducing possible artificial temporal phase change on the optimizing pixel's phase center.

The TP-ESM optimized interferogram of one baseline can be obtained by

$$I_{\text{TP-ESM}} = \overline{|S_{\text{vv}}|}^2 \cdot e^{i\phi_{\text{vv}}} + 4 \cdot \overline{|S_{\text{vh}}|}^2 \cdot e^{i\phi_{\text{vh}}} \quad (10)$$

where $I_{\text{TP-ESM}}$ is the TP-ESM optimized interferogram, ϕ_{vv} and ϕ_{vh} are, respectively, the corresponding interferometric phase of the VV and VH channels. $\overline{|S_{\text{vv}}|}$ and $\overline{|S_{\text{vh}}|}$ in (10) are, respectively, the temporal mean amplitude of VV and VH channels, which can be calculated as

$$\overline{|S_{vv}|} = \frac{1}{N}\sum_{i=1}^{N}|S_{\text{vv},i}|, \overline{|S_{\text{vh}}|} = \frac{1}{N}\sum_{i=1}^{N}|S_{\text{vh},i}| \quad (11)$$

where N is the number of PolSAR images, $S_{\text{vv},i}$ and $S_{\text{vh},i}$ represent VV and VH channel SLC of the ith PolSAR image. The coefficient 4 for the VH channel in (10) comes from the coefficient 2 before the VH channel in the Pauli basis scattering vector [see (2)], which is estimated to balance the intensity power between these two polarimetric channels [34]. Otherwise, the VV channel pixels' intensity values would be much bigger than that of VH channel for most pixels. In this case, the VH channel can hardly contribute to interferograms' optimizations.

It can be found that the proposed TP-ESM method is similar to the TP-MSM method, which both optimize interferograms by weighted summing of the corresponding VV and VH interferograms. However, the employed weights are different for TP-MSM and TP-ESM. Instead of taking the amplitudes of VV and VH interferogram as their weights for the optimization, the temporal mean VV and VH channel SAR images' amplitudes are employed for the weights' estimation in the proposed TP-ESM. This modification is made mainly due to two considerations. On the one hand, the ESM constraint should be applied for PolPSI applications to avoid introducing artificial phases on pixels' phase centers that maybe misinterpreted as deformation. On the other hand, the temporal mean amplitude is supposed to be able to better relate to the dominant SM along time, and it is less affected by the speckle noise than the interferograms' amplitudes. Although other choices, for instance, weighted mean amplitudes, could be employed to determine the weights in TP-ESM, the mean amplitude can represent all pixels' overall scattering behavior in the time dimension.

D. Polarimetric Persistent Scatterer Interferometry (PolPSI) Data Processing

Different PolPSI techniques can be developed based on different interferometric phase polarimetric optimization methods. Nevertheless, the data processing procedures are similar for these PolPSI techniques, and there are mainly four steps.

1) Data Preparation: First, the time-series PolSAR images are coregistered and cropped. Second, by employing the precise orbit data and an external digital elevation model (DEM), differential interferograms (with respect to a common master image) after removing the flat Earth and topographic phases are generated. Until now, the required data for the subsequent processing (f.i., the SLCs and scattering vectors) can be prepared.

2) Interferometric Phase Polarimetric Optimization: Then, based on the prepared data in the previous step, the different optimized interferogram stacks are separately obtained by using different polarimetric optimization methods in this step. In this study, ESPO, TP-MSM, and the proposed TP-ESM algorithms are used for the polarimetric optimization, separately.

3) Pixel Selection: Pixels with high interferometric phase quality should be identified for PSI processing. In this study, the temporal phase coherence (TPC) [11], [55] is to used select qualified pixels for all the PolPSI techniques. Specifically, first, for each interferogram stack, TPC of each pixel over all the interferograms is estimated as

$$\gamma_{\text{TPC}} = \frac{1}{M} \cdot \left|\sum_{i=1}^{M} e^{j\cdot\psi_{\text{noise},i}}\right| \quad (12)$$

where M is the number of interferograms, j is the imaginary unit, $\psi_{\text{noise},i}$ is the interferometric noise phase of the ith interferogram that can be estimated by the pixel's neighboring pixels [11], [55]. Then, by setting a TPC threshold, those pixels with TPC values

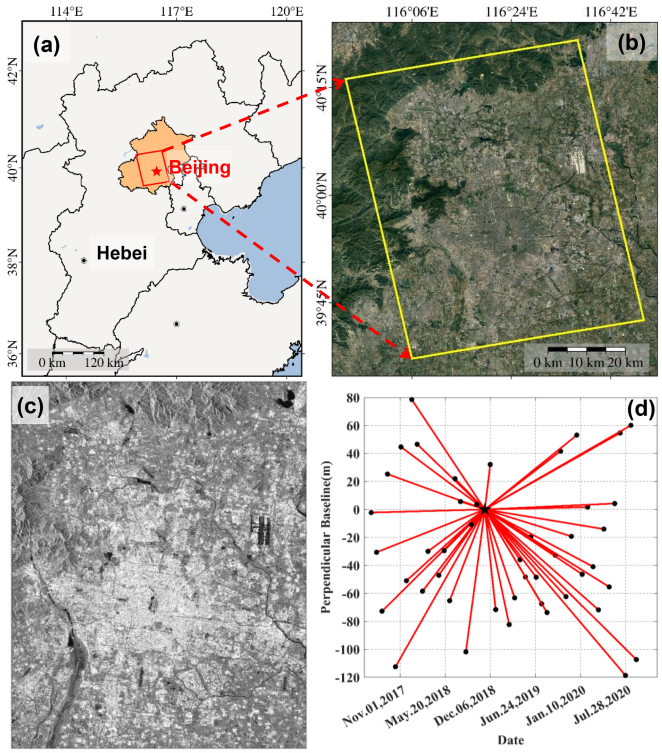

Fig. 1. (a) Location of the test area, the red rectangle indicates the SAR images' coverage. (b) Optical image over the test area. (c) Mean SAR amplitude image. (d) Temporal-spatial baselines of generated interferograms.

higher than this threshold can be recognized as qualified pixels for the subsequent PSI processing.

4) StaMPS Processing: The optimized interferograms and selected high quality pixels are the input of the PSI processing with StaMPS [11], [12]. After the PSI processing with StaMPS, which mainly consists of noisy pixel weeding, 3-D phase unwrapping, spatial-temporal filtering, and deformation velocity estimation, deformation time-series can be obtained for each PolPSI technique.

III. Test Area and Dataset

To test and assess the performance of the proposed TP-ESM method, 46 DP Sentinel-1 images acquired from June 2017 to September 2020 over Beijing are employed. All the PSI and PolPSI processings have been applied over $5300 \times 16\,500$ pixels in the study. Beijing is the capital city of China and has been suffering from ground deformation mainly caused by underground water extraction over the recent decades [49], [56], [57]. The location of the test area, the corresponding optical and temporal mean SAR amplitude images are shown in Fig. 1(a)–(c).

A Shuttle Radar Topography Mission DEM over the test area is used for the generation of differential interferograms. By employing the single master approach, 45 interferograms are obtained with the employed 46 SAR images, and their baselines are plotted in Fig. 1(d). It is worth to be noted that for the conventional PSI processing only VV channel SAR images are used, while both VV and VH SAR images are required for the PolPSI processing (with the TP-MSM, TP-ESM, or ESPO method).

IV. Results and Analysis

One PSI processing and three PolPSI processings (TP-MSM, TP-ESM, and ESPO method) have been carried out in this study to demonstrate the effectiveness of the proposed TP-ESM method. For PSI processing, same as conventional Sentinel-1 PSI applications, only the original VV channel interferogram stack is required. While for the three PolPSI processings, the three corresponding polarimetric optimized interferogram stacks are employed. Hereafter, the four methods are named as the VV, TP-MSM, TP-ESM, and ESPO method, respectively. In addition, to make a fair comparison of the four approaches obtained ground deformation results, the TPC method [55] with the threshold of 0.9 is used for the qualified pixels' selection for all the four approaches.

A. Interferogram Optimization Results Analysis

To analysis the PolPSI methods' performances on interferograms' optimization, together with the VV channel interferograms, the three PolPSI methods optimized interferograms with two different baselines over two subsections are depicted in Figs. 2 and 3, respectively. Fig. 2 shows the interferograms over the China National Olympic Sports Center [see Fig. 2(p) red rectangle] and the China National Stadium [see Fig. 2(p) yellow rectangle]. There are two groups of interferograms that, respectively, with a long [see Fig. 2(a)–(d)] and a short [see Fig. 2(e)–(h)] temporal baseline. For the VV interferogram with the long temporal baseline, which has been seriously affected by the spatial and temporal decorrelations, the edges of structures can hardly be seen. After being optimized by TP-ESM and ESPO, the shapes of the China National Olympic Sports Center and the China National Stadium become more clear. However, for the TP-MSM optimized interferogram, this improvement is insignificant. Same observations can be obtained from the interferograms with a short baseline [i.e., Fig. 2(e)–(h)]. Moreover, it can be found that TP-ESM and ESPO are with very similar optimization performances by comparing their results. This can be further confirmed by the TPC maps [see Fig. 2(i)–(l)], where the TP-ESM and ESPO related TPC values are similar and higher than that of VV and TP-MSM. For instance, over the edge of the China National Olympic Sports Center, which is like an elliptical ring, more pixels with TPC values close to 1 have been obtained by TP-ESM and ESPO than by VV and TP-MSM. Specifically, the percentages of pixels with TPC higher than 0.9 over this subsection are 4.2%, 2.6%, 5.6%, and 5.9% for the VV, TP-MSM, TP-ESM, and ESPO method, respectively.

This interferogram optimization ability difference between TP-ESM and TP-MSM is mainly caused by the different weighting strategies used for these two methods [see (9) and (10)]. Specifically, in the TP-MSM method, the polarimetric optimization weights of VV and VH channel interferograms are determined by the amplitudes of two SLCs forming the VV and VH channel interferograms, respectively. For the C-band medium resolution Sentinel-1 SAR images, amplitudes are

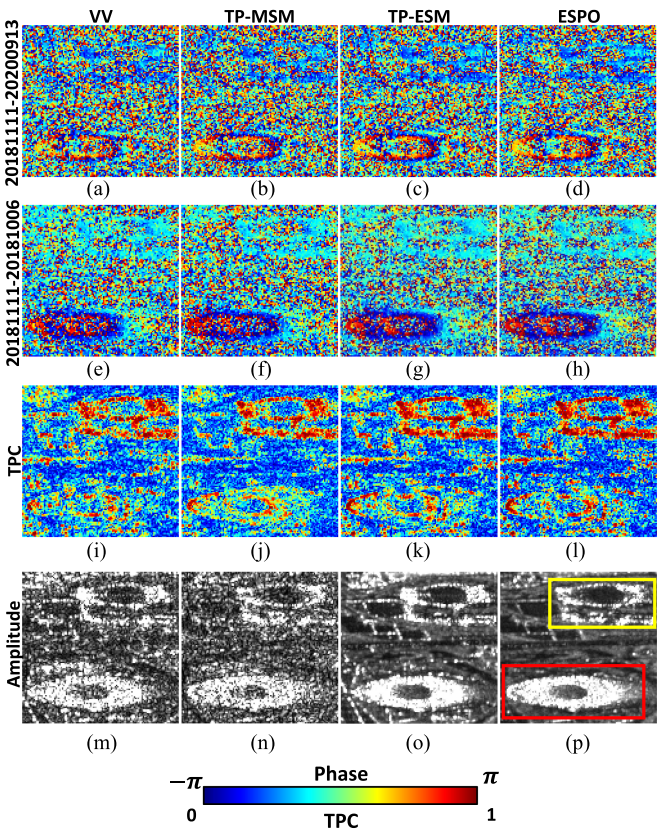

Fig. 2. First and second rows are the subsection interferograms with the long and short temporal baseline derived by the VV [(a) and (e)], TP-MSM [(b) and (f)], TP-ESM [(c) and (g)] and ESPO [(d) and (h)] method, respectively. The location of the subsection is indicated by the white rectangle A in Fig. 7. The third row shows the TPC maps related to different methods. The last row is the amplitude image of the master VV SLC (m), master VH SLC (n), temporal mean VV amplitude (o) and temporal mean VH amplitude (p), respectively.

easily affected by the speckle and appear noisy. Thus, the weights determined by the two SLCs' amplitude in TP-MSM are unstable and may not represent the different SMs of each polarimetric channel, resulting in the unsatisfied optimization performance. The VV and VH amplitude of the master image is shown in Fig. 2(m) and (n), where the shapes of structures have been blurred by the heavy speckle noise. On the other hand, the proposed TP-ESM method takes the square of the temporal mean amplitude (under Pauli basis) of VV and VH SAR images as their optimization weight, respectively. Therefore, the speckle noise can be significantly reduced and the temporal stable SMs be better represented than that of TP-MSM. The temporal mean VV and VH amplitude images depicted in Fig. 2(o) and (p) prove this point, where different powers of various features can be easily distinguished between the two polarimetric channels.

The second subsection is located over a group of buildings (indicated by the white rectangle B in Fig. 7), where subsidence happened during the observation period. By comparing the interferograms before and after optimization with the two baselines, the same observations with that from Fig. 2 can be obtained. In addition to the better structures' edges preservation abilities of TP-ESM and ESPO than the VV and TP-MSM over interferograms, the deformation fringes are better retrieved [see Fig. 3(c) and (d)]. The corresponding TPC and amplitude maps in the third and fourth rows in Fig. 3 support this observation. In specific, the percentages of pixels with TPC higher than 0.9 over this subsection are 2.3%, 1.8%, 3.5%, and 3.6% for the VV, TP-MSM, TP-ESM, and ESPO method, respectively.

To analysis the phase quality optimization performances of the different methods on all the generated interferograms, the TPC histograms corresponding to the whole test area [see Fig. 1(a)–(c), over $5300 \times 16\,500$ pixels] of all the four methods are shown in Fig. 4. It can be found from Fig. 4(a) and (b) that there are more pixels with TPC higher than 0.9 of ESPO and TP-ESM interferograms than that of VV and TP-MSM results. More specifically, according to Fig. 4(c) and (d), the pixels with TPC higher than 0.9 account for around 2.9%, 2.7%, 2.0%, and 1.1% for the ESPO, TP-ESM, VV, and TP-MSM result, respectively. This indicates that the overall interferometric phase optimization ability ranking of the three PolPSI methods is ESPO $>$ TP-ESM $>$ TP-MSM.

By employing different thresholds, different numbers of high quality pixels can be identified by different methods over the whole test area, as it is shown in Table I. For all the used TPC threshold, from 0.7 to 0.95, TP-ESM and ESPO are able to improve the density of selected qualified pixels for ground deformation monitoring w.r.t. VV approach. On the other hand, TP-MSM decreases the percentages of the high quality pixels w.r.t. VV approach. With lower TPC threshold, i.e., 0.7 and 0.8, TP-ESM performances as well as or better than ESPO on the density of selected pixels. Moreover, the number of relatively high quality pixels (with TPC higher than 0.9 or 0.95) for the TP-ESM method is close to that of ESPO, which accounts for around 94% of ESPO obtained pixels' numbers. In addition, for TP-ESM and ESPO, higher TPC threshold values are with more significant improvements on selected pixel density w.r.t. that of the VV approach. This indicates that for high precision ground deformation monitoring applications, the TP-ESM and ESPO approaches are more effective and necessary w.r.t. to the conventional VV approach.

To further demonstrate the good performances of the proposed TP-ESM method on high quality pixels' phase noise reduction, the pixels with ESPO TPC higher than 0.9 (named as ESPO selected pixels in this article) are selected, and their interferometric phases obtained by the four methods over the second subsection are shown in Fig 5. As the black circles in Fig. 5 indicate, many noisy pixels in the VV approach interferograms have been optimized by employing the TP-ESM method. More importantly, these TP-ESM optimized pixels' interferometric phase values are very similar to that of ESPO.

To analysis phase differences over the ESPO selected pixels (with ESPO TPC higher than 0.9) between ESPO and the other three employed approaches, the IMPD values for the interferogram pair (ESPO and TP-MSM), (ESPO and TP-ESM), and (ESPO and VV) have been calculated over the whole test area. Specifically, the IMPD value is calculated for each interferogram as follows:

$$\mathrm{IMPD} = \frac{1}{N}\sum_{i=1}^{N} |\phi_{\mathrm{ESPO},i} - \phi_{\mathrm{App.},i}| \tag{13}$$

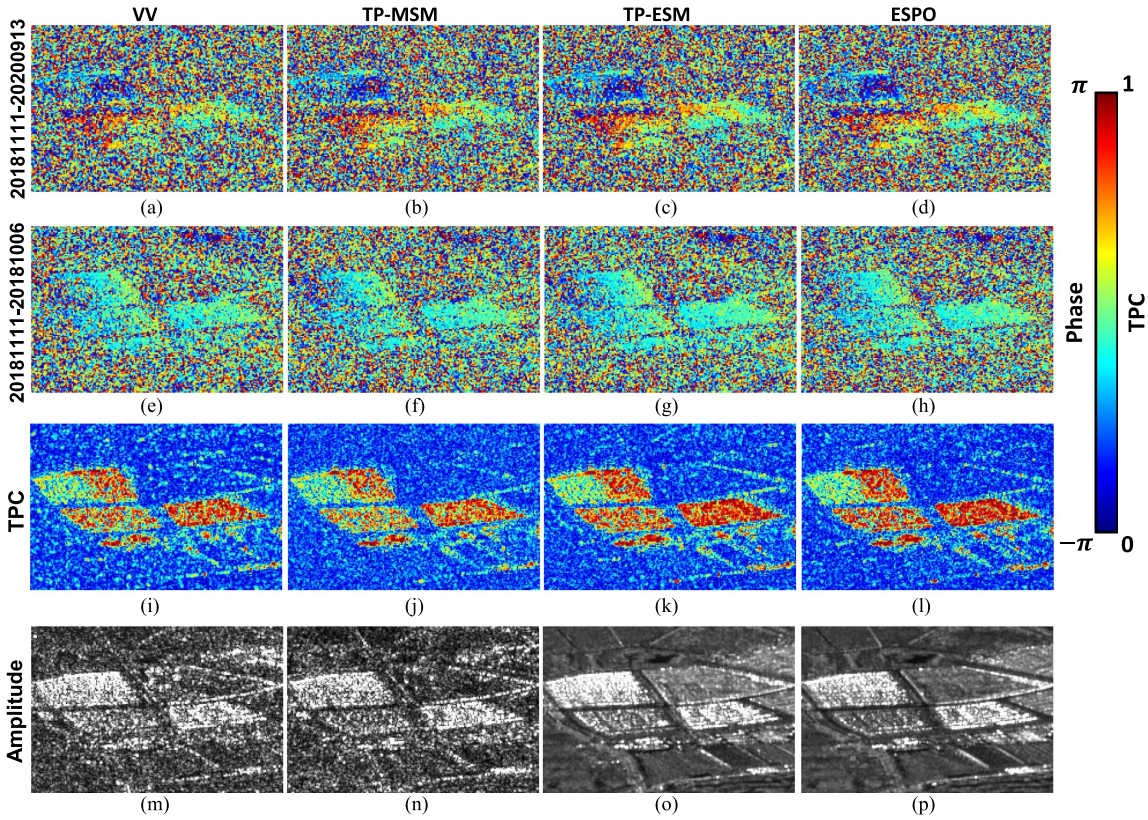

Fig. 3. First and second rows are the subsection interferograms with the long and short temporal baseline derived by the VV [(a) and (e)], TP-MSM [(b) and (f)], TP-ESM [(c) and (g)] and ESPO [(d) and (h)] method, respectively. The location of the subsection is indicated by the white rectangle B in Fig. 7. The third row shows the TPC maps related to different methods. The last row is the amplitude image of the master VV SLC (m), master VH SLC (n), temporal mean VV amplitude (o) and temporal mean VH amplitude (p), respectively.

TABLE I
NUMBER OF HIGH QUALITY PIXELS OBTAINED BY USING DIFFERENT POLARIMETRIC OPTIMIZATION APPROACHES WITH DIFFERENT TPC THRESHOLDS OVER THE WHOLE TEST AREA

Th. / App.	0.7	0.8	0.9	0.95
VV	7 114 369 (0%) / (87%)	4 190 372 (0%) / (78%)	1 754 696 (0%) / (69%)	712 872 (0%) / (67%)
TP-MSM	5 018 809 (–29%) / (61%)	2 736 057 (–35%) / (51%)	992 835 (–43%) / (39%)	318 524 (–55%) / (30%)
TP-ESM	8 509 048 (20%) / (104%)	5 307 808 (27%) / (98%)	2 377 339 (35%) / (93%)	998 734 (40%) / (94%)
ESPO	8 165 277 (15%) / (100%)	5 399 675 (29%) / (100%)	2 547 588 (45%) / (100%)	1 059 392 (49%) / (100%)

"App." and "Th." are the abbreviations of "Approach" and "Threshold," respectively. "$N(i\%)/(j\%)$" in the table represent the number of selected high quality pixels (N), its increase or decrease ($i\%$) w.r.t. that of the VV approach and its percentage ($j\%$) w.r.t. the number of pixels selected by the ESPO method, respectively.

where N, $|\ \ |$, $\phi_{\text{ESPO},i}$, and $\phi_{\text{App.},i}$ represent the number of the ESPO selected pixels, absolute value operation, the ith selected pixel's phase obtained by ESPO, and one of the three comparing approaches (i.e., VV, TP-MSM, or TP-ESM), respectively. It should be noted that IMPD is calculated from one interferogram pair to the other, and a total of 45 IMPD values can be obtained for each comparing approach. All the IMPD values have been depicted in Fig. 6.

As Fig. 6 demonstrates, for all the interferograms, the IMPD values between the proposed TP-ESM and ESPO are the lowest among the three comparing methods (i.e., VV, TP-MSM, and TP-ESM). On the other hand, the performance of TP-MSM is not stable. Compared with VV interferograms, TP-MSM decreases phase quality for 29 interferograms, and for the other 16 interferograms it obtains similar results to the VV approach. The temporal mean of the IMPD values for the (ESPO and TP-MSM), (ESPO and TP-ESM), and (ESPO and VV) pair is 0.4199, 0.2076, and 0.3270, respectively. Taking the ESPO derived phase as the reference, the average phase quality improvement of the proposed TP-ESM method w.r.t. VV approach is around 36.51%; while the counterpart for TP-MSM is around -28.41% (minus means decrease on pixels phase qualities).

B. Ground Deformation Results Analysis

The ground deformation monitoring results obtained by the four approaches with different interferogram stacks (VV or optimized ones) and the identical qualified pixels identification

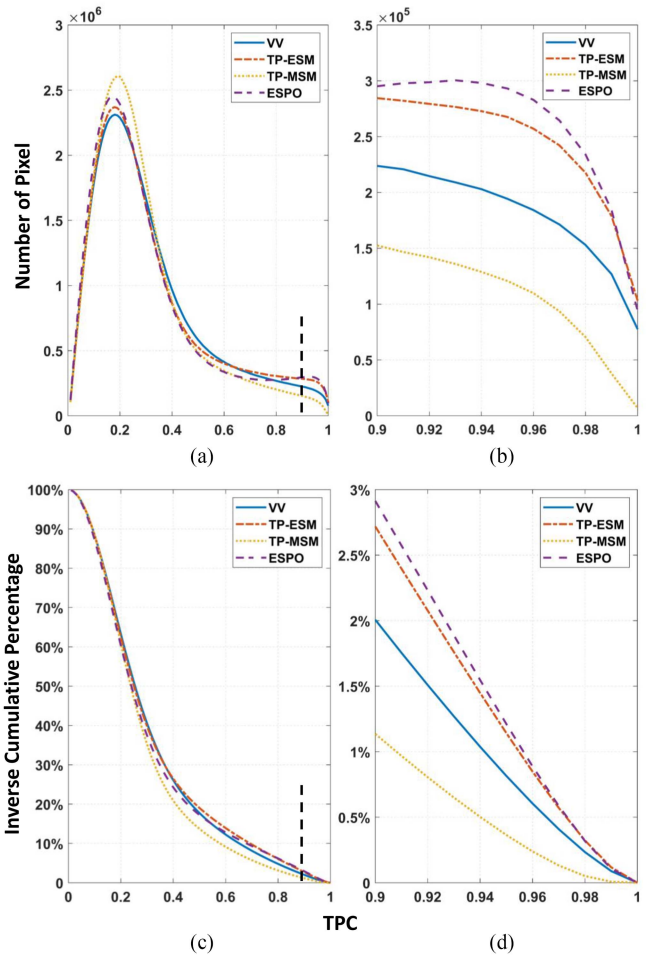

Fig. 4. (a) and (c) TPC and TPC inverse cumulative percentage histograms related with the four methods' interferograms. (b) and (d) is the detailed zoom of (a) and (c) for TPC values from 0.9 to 1, respectively. The black dashed lines in (a) and (c) indicate the TPC threshold (i.e., 0.9) for the selection of qualified pixels.

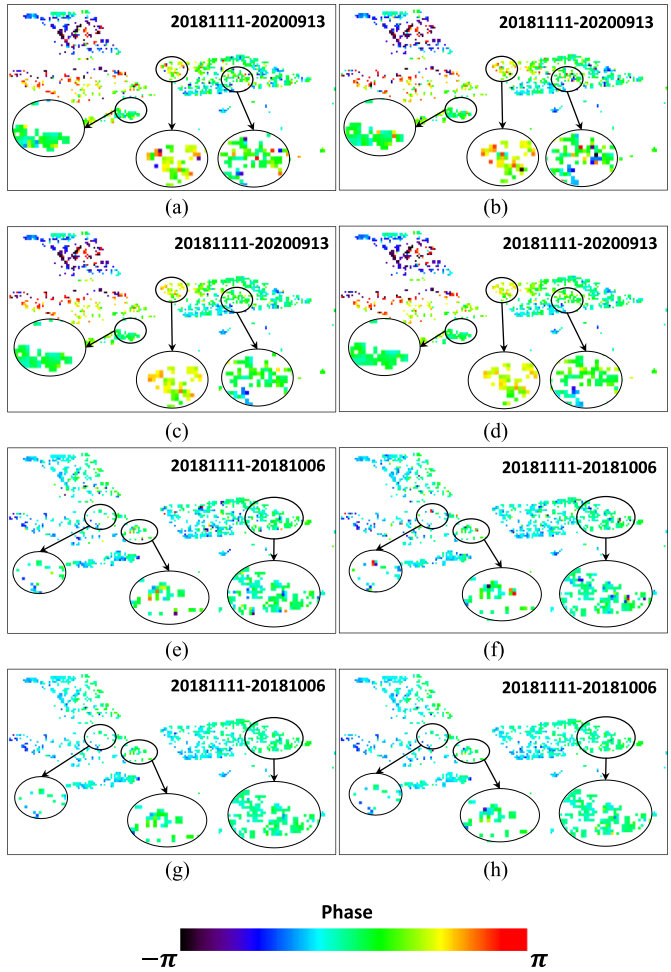

Fig. 5. Interferometric phases obtained by different methods of the selected pixels with ESPO TPC higher than 0.9 over the second subsection. (a)–(d) and (e)–(h) are from the interferograms with the temporal baseline 20181111-20200913 and 20181111-20181006, respectively. The black circles highlight the pixels whose phase noises have been reduced via optimization with TP-ESM and ESPO.

method (i.e., TPC higher than 0.9) are depicted in Fig. 7. It can be observed from Fig. 7 that the overall ground deformation patterns retrieved by the four methods are in coincidence with each other. During the observation period (from June 2017 to September 2020), there are mainly three subsidence bowls surrounding the central district of Beijing, with one located in the north-west and the other two south-east.

The main faults over the test area have also been plotted in Fig. 7(d). In general, the fault traces are close to the subsidence boundaries, which suggests the ground deformation over the test area is affected by these geological faults. This is very evident in the subsection C, where the up-left and down-right ground deformations are separated by the fault [see Fig. 7(e) and (f)]. In addition, as the black circles in Fig. 7(g) and (h) demonstrate, more details of subsidence along the fault can be retrieved by the TP-ESM than VV approach.

Thanks to the obtained higher pixel densities, more details of the terrain displacements can be observed from the TP-ESM and ESPO results than that from VV and TP-MSM. Specifically, the final number of ground deformation monitoring pixels is 1 740 206, 986 217, 2 356 268, and 2 492 681 for the VV, TP-MSM, TP-ESM, and ESPO result, respectively. The improvement on pixel density w.r.t. that of VV achieved by the proposed TP-ESM and ESPO is 35% and 43%, respectively. On the other hand, the TP-MSM obtained fewer pixels (with a decrease of 43%) than the VV approach over the test area, indicating it is not applicable on Sentinel-1 data. As expected, these results are consistent with the analysis of interferograms, since better interferometric phase quality or better interferometric phase optimization performances always lead to better PSI processing results.

The maximum ground deformation velocity reaches up to around −80 mm/yr at the center of these subsidence bowls, which is mainly caused by the underground water extractions [56], [57], [58]. Considering the groundwater data over the test area has been measured at the end of each year, the data for 2017 and 2019 are employed for the analysis (Beijing Water Authority, http://swj.beijing.gov.cn/zwgk/sjfb/). In general, the groundwater storages over Beijing are respectively 17.74 and

TABLE II
STATISTICAL ANALYSIS OF THE VV AND TP-ESM METHOD RETRIEVED GROUND DEFORMATION RESULTS OVER BEIJING

Deformation Velocity	VV P.N.	TP-ESM P.N.	P.N. Impro.	Add. Area
>0 (mm/yr)	1133310	1532041	398731 (35.18%)	3987.31 hm^2
0 to −10 (mm/yr)	370832	503283	132451 (35.72%)	1324.51 hm^2
−10 to −20 (mm/yr)	139499	187872	48373 (34.68%)	483.73 hm^2
−20 to −40 (mm/yr)	82384	114244	31860 (38.67%)	318.6 hm^2
−40 to −60 (mm/yr)	12131	16382	4251 (35.04%)	42.51 hm^2
−60 to −80 (mm/yr)	2050	2446	396 (19.32%)	3.96 hm^2

"VV P. N.", "TP-ESM P. N.", "P. N. Impro.", and "Add. Area" in the table represent the VV method obtained pixels' number, TP-ESM obtained pixels' number, TP-ESM achieved pixels' number improvement with respect to that of the VV method, and the additional area monitored by TP-ESM with respect to that of the VV method, respectively.

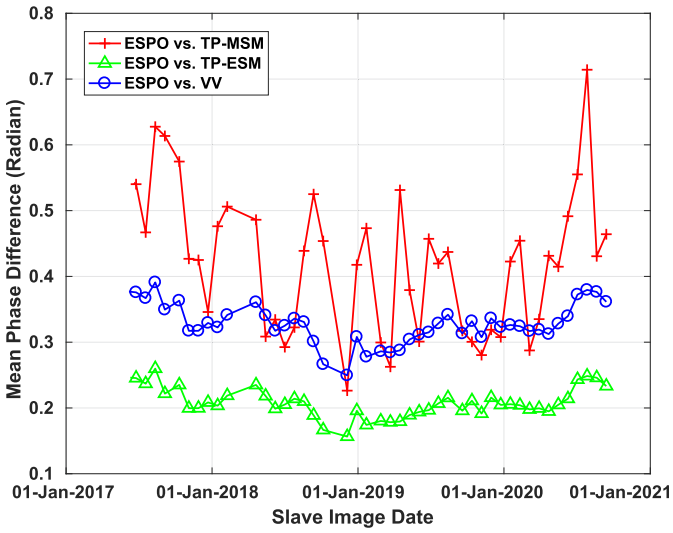

Fig. 6. IMPD between ESPO and the other three approaches over the ESPO selected pixels (ESPO TPC higher than 0.9). As the interferogram is generated with the single-master method, they can be represented by their slave image date as the X-axis shows. The red cross, green triangle and blue circle represent the interferogram level mean phase difference (IMPD) values between the interferogram pair (ESPO and TP-MSM), (ESPO and TP-ESM), and (ESPO and VV), respectively.

15.95 billion cubic meters in 2017 and 2019, indicating a decrease of groundwater storage. The groundwater level at 2017 and 2019 together with the main subsidence bowls (indicated by the white circles) have been shown in Fig. 8. It can be seen from Fig. 8 that ground subsidence in general happened around the subsections where the groundwater draw-down. Nevertheless, the spatial patterns of subsidence are different with that of the groundwater draw-down. This is due to that the ground subsidence was triggered by groundwater draw-down, but confined and diversified by the compressible sediments and other geological factors [59], which are out of the scope of this study.

The numbers of qualified pixels obtained by the VV and TP-ESM method with different deformation velocity ranges are listed in Table II. It can be observed from Table II that, for all the ranges of deformation velocity, the proposed TP-ESM can obtain more pixels than the VV method. This indicates that TP-ESM is able to improve the ground deformation monitoring ability w.r.t. the VV method independent of the ground deformation magnitude over the test area. For the areas suffering from relatively large subsidence, i.e., with deformation velocity range (−40 to −60 mm/yr) and (−60 to −80 mm/yr), the pixel density improvements achieved by TP-ESM w.r.t. VV are 35.04% and 19.32%, respectively. In other words, more areas with significant subsidence or more subsidence details over the test area can be retrieved by the TP-ESM w.r.t. VV. Specifically, as shown in Table II, the extra significant subsidizing areas (with subsidence velocity larger than 40 mm/yr) detected by TP-ESM are around 46 hm^2 w.r.t. that of the VV method.

To further analysis the SMs of the increased pixels achieved by TP-ESM w.r.t. VV, their H-Alpha plot together with all TP-ESM obtained pixels' H-Alpha plot [52], [60] have been depicted in Fig. 9. As the red rectangle in Fig. 9(a) highlights, the increased pixels' entropy and alpha values are centered around 0.5 and 45°, respectively. This means these increased pixels are mainly behaving as medium entropy multi-SMs, which are usually corresponding to building regions with multiple scattering over the test area [52]. On the other hand, as shown in Fig. 9(b), a majority of the ground deformation monitoring pixels retrieved by TP-ESM are with low entropy and alpha values, mainly corresponding to surface scatterers. The abovementioned analysis infers that the additional pixel achieved with TP-ESM w.r.t. VV are pixels mainly related to building regions with multiple scattering.

Based on the land cover map of 2020 over the test area produced by the ESA (i.e., ESA WorldCover 10 m 2020, https://esa-worldcover.org/en), the abovementioned increased pixels can be classified into different categories. As the result, these additional pixels are categorized into mainly three land cover types, where the built-up, tree cover, and cropland/bare vegetation account for around 83%, 13%, and 4%, respectively. The results confirm that the additional pixels obtained by TP-ESM w.r.t. VV are mainly related to building regions with multiple scattering mechanisms (MSMs). When TP-ESM is employed, the decorrelations caused by MSMs over these regions can be reduced w.r.t. single VV channel, leading to the increase in qualified pixels' density.

Detailed ground deformation monitoring results of the VV, TP-ESM, and ESPO approaches over the two subsections [highlighted by the white rectangle A and B in Fig. 7(a)] are shown in Fig. 10. Within the first subsection, the proposed TP-ESM is able to obtain more qualified pixels than the VV approach for

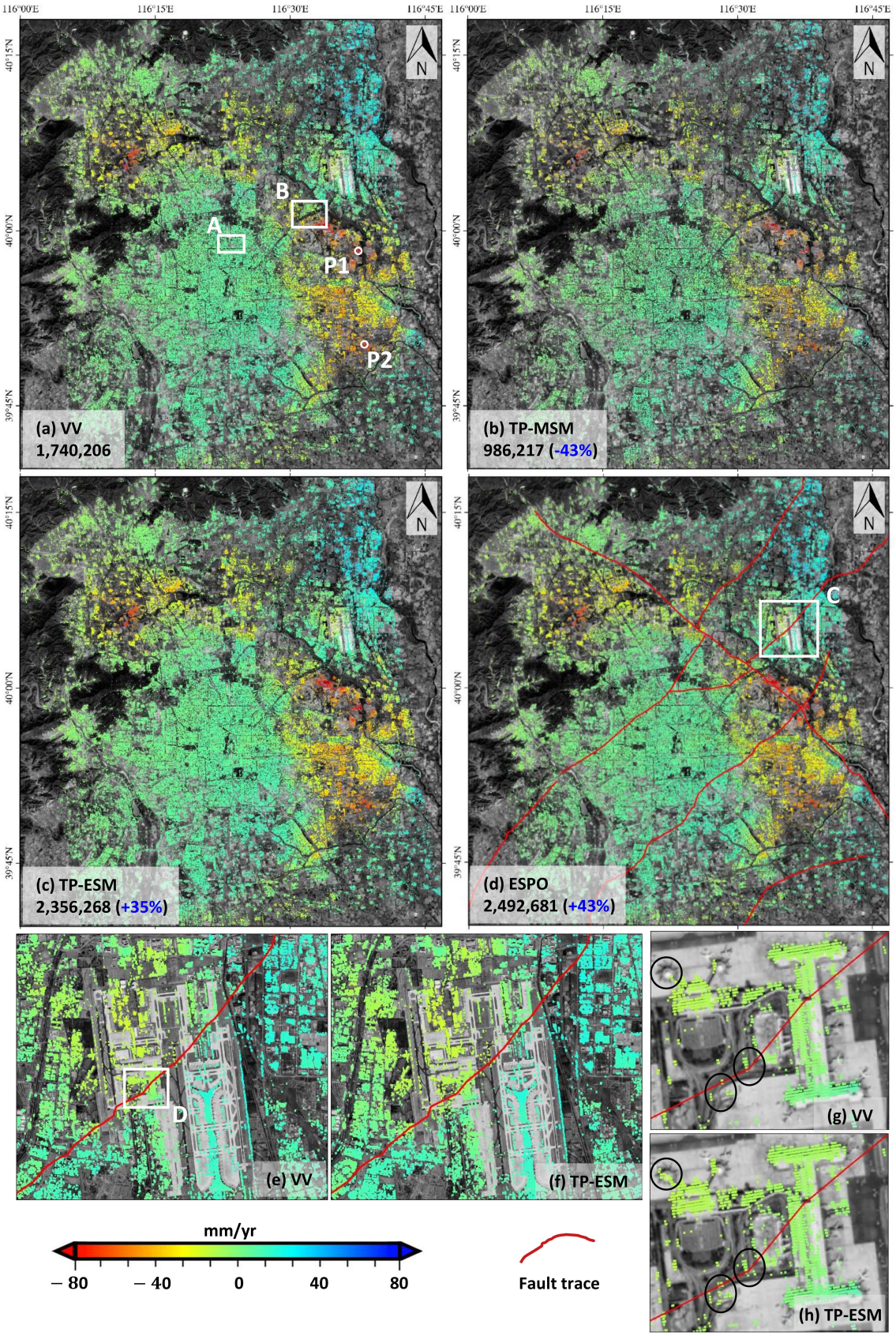

Fig. 7. Ground deformation velocity estimated by the (a) VV, (b) TP-MSM, (c) TP-ESM, and (d) ESPO approach, respectively. The numbers in (a, b, c, and d) represent, respectively, the final numbers of pixels obtained by the four approaches, and the increase or decrease percentage in the bracket is calculated by taking the VV approach as a reference. (e) and (f) Details of VV and TP-ESM results over the subsection C [see the white rectangle in (c)], (g) and (h) Detailed zooms over the subsection D [see the white rectangle in (e)] for VV and TP-ESM results, respectively.

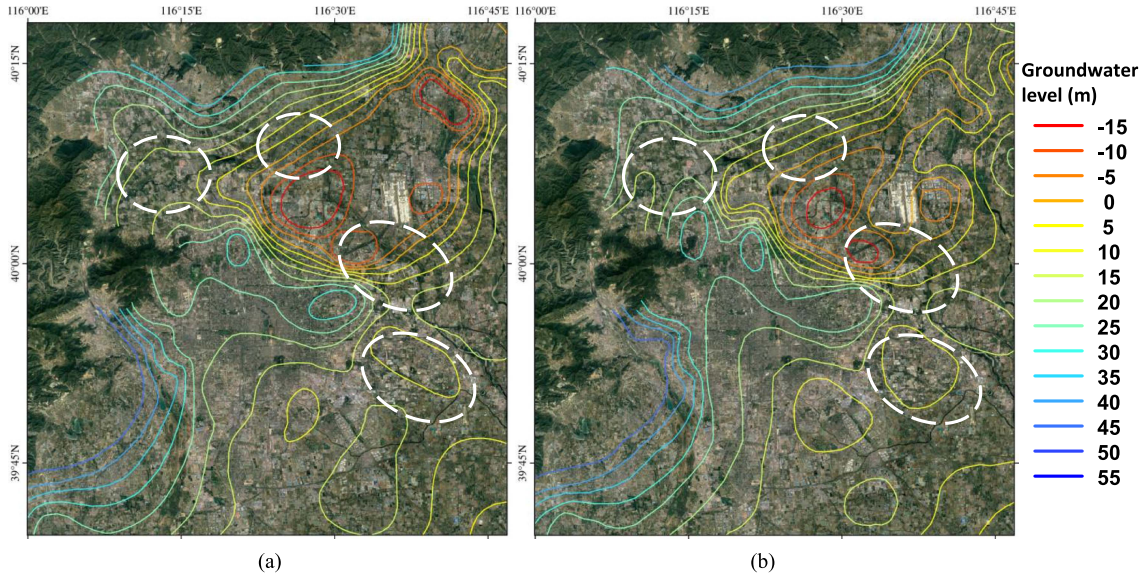

Fig. 8. Groundwater level of (a) 2017 and (b) 2019 over the test area. The white circles indicate the locations of the main subsidence bowls over the test area.

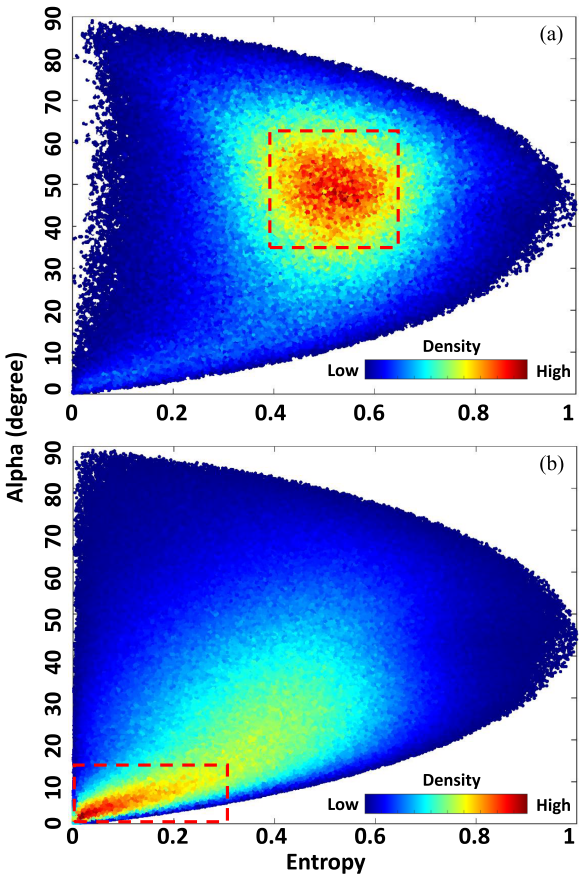

Fig. 9. (a) and (b) H-Alpha plots for the TP-ESM obtained extra pixels w.r.t. the VV method and the TP-ESM obtained pixels.

deformation monitoring around the China National Olympic Sports Center (white rectangle A), the China National Stadium (white rectangle B) and the China National Aquatics center (white rectangle C). For the second subsection, there are subsidence areas and more deformation details or pixels have been obtained by TP-ESM than the VV method as the white rectangles D, E, and red dashed line are highlighted. As expected, ESPO slightly outperforms the proposed TP-ESM over these two subsections on the final pixel density. However, by considering the very high computation burden of ESPO [46], [48], [49], the proposed TP-ESM, which is with relatively very small or negligible computation cost (see Section V–C), has achieved quite satisfactory results.

The deformation time-series retrieved by the four employed methods over the two selected pixels located in the two subsidence subareas [i.e., P1 and P2 as shown in Fig. 7(a)] have been depicted in Fig. 11. It can be observed from Fig. 11 that the time-series deformations obtained by the proposed TP-ESM are consistent with the other three, indicating the reliability of TP-ESM in the monitoring of time-series ground deformation. The two pixels suffered from nearly linear sinking during the observation period and the maximum cumulative subsidence reach up to around 220 mm and 180 mm for P1 and P2, respectively.

To analysis the relationship between deformation time-series with rainfall, the TP-ESM obtained time-series deformation of P1 together with the corresponding monthly rainfall data has been depicted in Fig. 12. It can be observed from Fig. 12 that the ground subsidence velocity decreased from around September 2019 as the red line (linear fitting 1) and the blue line (linear fitting 2) demonstrate. This indicates that the increased rainfall in 2019 w.r.t. 2017 and 2018 (see the green line and the filled blue areas in Fig. 12) contributes to the decline of the subsidence velocity.

V. Discussion

A. VV and VH Channels' Contributions on the Optimization of the Proposed TP-ESM

It can be observed from (9) that the weights (or contributions) of VV and VH channels on the TP-ESM's optimization are

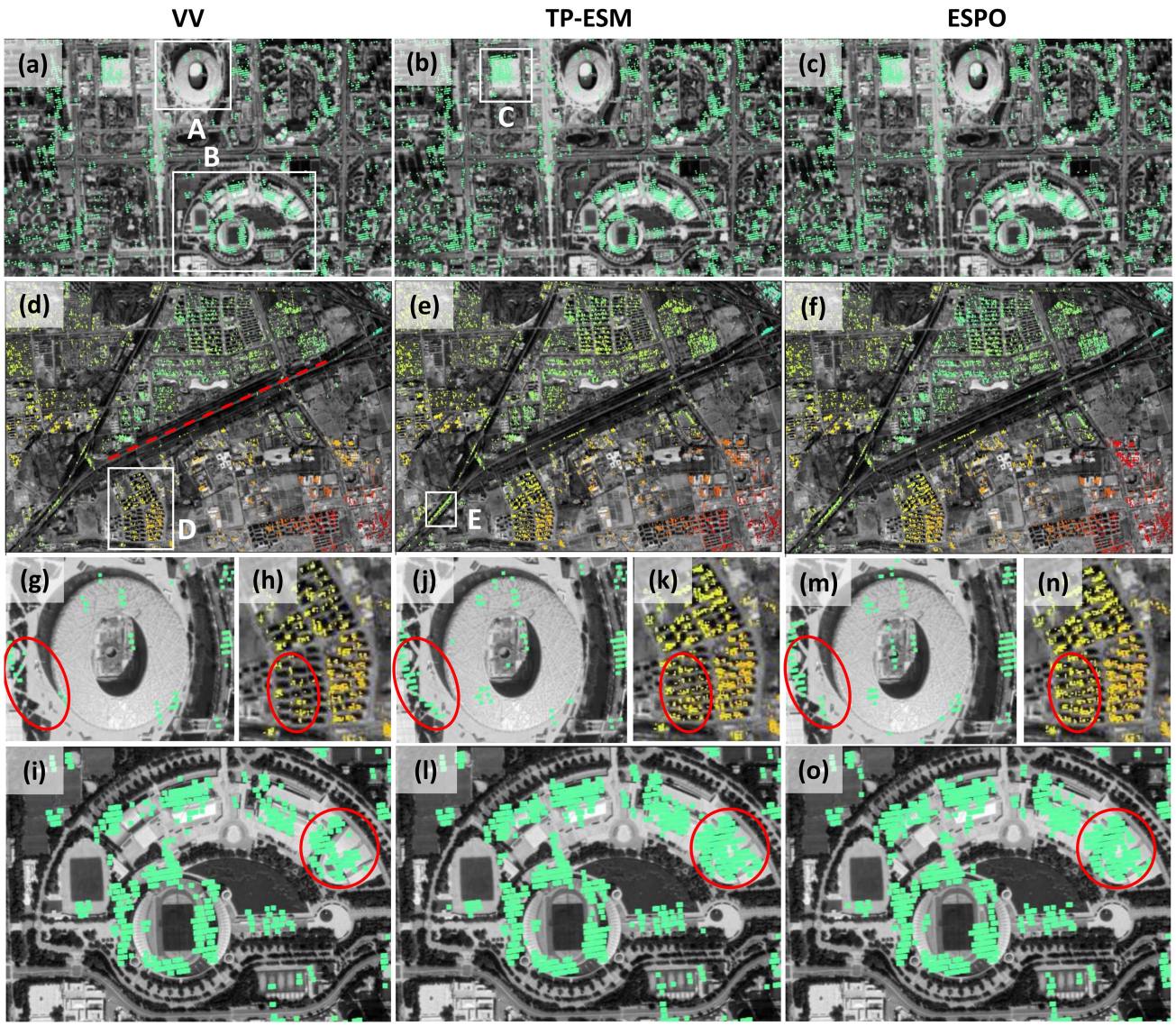

Fig. 10. Ground deformation velocity over the two subsections A and B [highlighted in Fig. 7(a)] estimated by the VV, TP-ESM and ESPO approach, respectively. The white rectangles and red dashed line in the figure indicate the areas where the proposed TP-ESM obtained more density of pixels than the VV approach. The subarea A, B in (a) and D in (d) have been enlarged below for each method derived results for better visualization, where the red circles indicate the subsections that TP-ESM outperforms the VV method.

determined by their temporal mean amplitudes. For pixels with ESM-TPC (TPC calculated with TP-ESM interferograms) higher than 0.9 (i.e., the TP-ESM selected pixels), the corresponding $\overline{|S_{\mathrm{vv}}|}^2$ (VV channel weight) and $4 \cdot \overline{|S_{\mathrm{vh}}|}^2$ (VH channel weight) have been compared. There are around 23.2% of the TP-ESM selected pixels with the VH channel weight bigger than their VV channel weight. This indicates that, in the test area, the VH channel contributes more to the TP-ESM optimizations of this 23.2% of the selected pixels than the VV channel. Thus, the VH channel contributes to the TP-ESM optimization results, and for some pixels, it plays a more important or determinant role than the VV channel.

To analysis the source of these 23.2% pixels, the H-Alpha plots for TP-ESM selected pixels with $4 \cdot \overline{|S_{\mathrm{vh}}|}^2 > \overline{|S_{\mathrm{vv}}|}^2$ and $4 \cdot \overline{|S_{\mathrm{vh}}|}^2 \leq \overline{|S_{\mathrm{vv}}|}^2$ are depicted in Fig. 13(a) and (b), respectively. For pixels that VH channel contributes more to the polarimetric optimization of TP-ESM, their entropy mainly ranges from 0.2 to 0.6, alpha from 45° to 60° [see Fig. 13(a)]. This indicates the 23.2% pixels are related to the medium entropy multiple scattering events (equals to a kind of volume scattering), which are mainly corresponding to building regions with MSMs over the test area. This could be caused by the building orientation or the complicated building structures over these subsections [61], [62], [63], where VH Chanel can better represent this kind of SM than VV. On the other hand, over the pixels that VV channel plays more important role [see Fig. 13(b)], their entropy and alpha values are mainly close to zero. This infers that these pixels mainly behave as low entropy surface scattering events [52], [60].

By following (13), the IMPD values between the interferogram pair (TP-ESM, VV) and (TP-ESM, VH) over all the interferograms can be calculated. However, for the IMPD values'

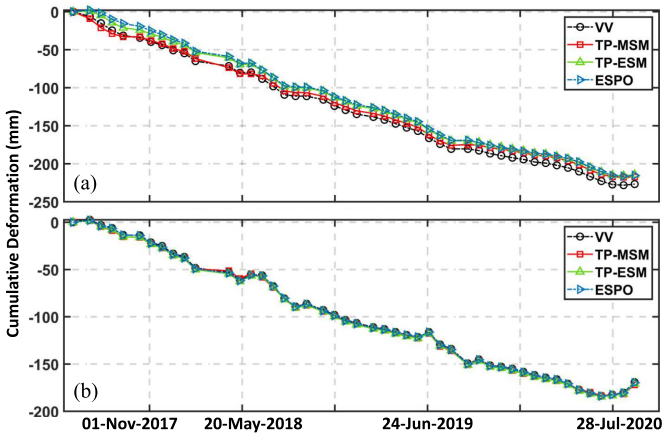

Fig. 11. Ground deformation time-series retrieved by the employed four methods over the two selected pixels (a) P1 and (b) P2. The locations of P1 and P2 are highlighted with the white circles in Fig. 7(a).

calculation of the (TP-ESM, VV) pair, only the pixels with the VV channel weight higher than VH are used. Meanwhile, the other pixels are used to calculate IMPD values for the (TP-ESM, VH) pair. The IMPD values over all interferograms for the two comparing pairs have been depicted in Fig. 14.

As Fig. 14 demonstrates that the IMPD values of the (TP-ESM, VV) pair are smaller than that of the (TP-ESM, VH) pair for all interferograms. This indicates that, in general, the VV channel determines more than the VH channel on pixels' TP-ESM optimization. This is mainly caused by the overall higher amplitudes (in Pauli basis) of the VV channel, and it is reasonable as higher amplitudes usually correspond with higher phase qualities. The IMPD variations along the slave image time (i.e., X-axis) are similar for both interferogram pairs, and the variations are mainly caused by the different decorrelations levels of different interferograms. In general, the interferograms with shorter temporal baselines (less temporal decorrelations) have smaller IMPD values, indicating phase noise also contributes to the TP-ESM optimization results. Nevertheless, high quality pixels' TP-ESM optimization results are mainly determined by the VV and VH channels, which can be validated by the very small IMPD value (i.e., 0.0844) of (TP-ESM, VV) pair over the interferogram with the shortest temporal baseline (i.e., with the slave image data of December 5, 2018).

B. DS Pixels' Optimization Effect of the Proposed TP-ESM

The ESPO method optimizes pixels via the D_A index, which is an effective phase quality metric for PS pixels' optimizations. On the other hand, the proposed TP-ESM does not rely on any interferometric phase quality metric for pixels' polarimetric optimizations. Therefore, it can be anticipated that the proposed TP-ESM outperforms ESPO on DS pixels' optimization. To validate the anticipation, numbers of ESPO and TP-ESM related high TPC pixels, which are selected from the pixels with both VV and VH D_A higher than 0.4, have been shown in Table III. As most of PS Pixels are with VV or VH D_A smaller than 0.4 [7], thus, the pixels with both VV and VH D_A higher than 0.4 can be treated as DS pixels for the validation.

TABLE III
NUMBER OF HIGH QUALITY PIXELS OBTAINED BY USING VV, TP-ESM, AND ESPO WITH DIFFERENT TPC THRESHOLDS OVER THE DS PIXELS

App. \ Th.	0.7	0.8	0.9
VV	3 006 068 (3%)	1 020 686 (1%)	130 116 (0.1%)
ESPO	3 367 012 (12%)	1 380 172 (35%)	190 047 (46%)
TP-ESM	3 799 020 (26%)	1 444 517 (42%)	206 748 (59%)

"App." and "Th." are the abbreviations of "Approach'" and "Threshold," respectively. *N* (*i*%)' in the VV column is the number of TPC selected pixels (*N*) and its percentage (*i*%) of all the pixels. "*N* (*i*%)" in the ESPO and TP-ESM columns represent the number of TPC selected pixels (*N*) and its increase (*i*%) w.r.t. that of the VV method, respectively.

It can be observed from Table III that TP-ESM can obtain more high quality pixels than ESPO for the different TPC thresholds (from 0.7 to 0.9) over the defined DS pixels (i.e., pixels with both VV and VH D_A higher than 0.4 in this subsection). In specific, the improvement on qualified DS pixel density achieved by ESPO and TP-ESM w.r.t. that of VV is (12%, 26%), (35%, 42%), and (46%, 59%) for the TPC threshold 0.7, 0.8, 0.9, respectively. Therefore, as the results over the test area indicate, the proposed TP-ESM performs better than the ESPO method with D_A on DS pixels' optimizations.

C. Polarimetric Optimization Computational Cost of the Porposed TP-ESM

The computation burden is an important metric to assess the overall performance of one PolPSI technique, and ESPO is with the best polarimetric optimization results in this study, which is also with the highest computation cost. Specifically, in this study, the ESPO method is implemented with MATLAB R2016b on a workstation equipped with an 8 core Intel (R) Xeon (R) Gold 5222 processor and 256 GB of RAM. The searching interval of the optimum parameters (i.e., α and ψ) of ESPO is set as 3°, and no parallel processing has been employed. Under this circumstance, it takes around 100 h for ESPO to optimize the $5300 \times 16\,500$ pixels over the test area.

On the other hand, the proposed TP-ESM method is with negligible computation cost w.r.t. that of ESPO, which takes less than 1 h for the same amount of pixels' optimization over the test area with the same implementation as ESPO. This high efficiency of the proposed TP-ESM is due to that it optimizes pixels by a weighted sum strategy [as shown in (10)]. Thus, it does not require the exhaustive search in a solution space for the optimum parameters for each pixel, which is computationally intensive. Moreover, TP-ESM achieves an improvement of 35% on ground deformation monitoring pixel density w.r.t. VV approach, which is just 8% less than ESPO (43%) related improvement over the test area. This indicates the proposed TP-ESM method is a cost-effective PolPSI algorithm, thus, it is more applicable than ESPO for PolPSI applications over large study areas.

D. Applying the Proposed TP-ESM on Other PolSAR Datasets

Limited by the available time-series PolSAR images, the proposed TP-ESM has only been applied and tested on the DP

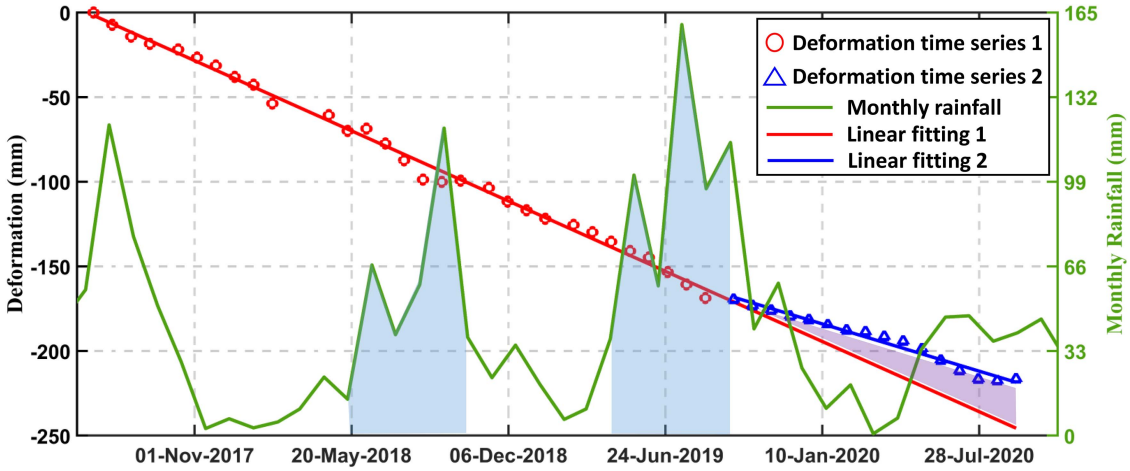

Fig. 12. Relationship between the ground deformation time-series and the rainfall over the pixel P1. The location of the selected pixel P1 is highlighted with the white circles in Fig. 7(a).

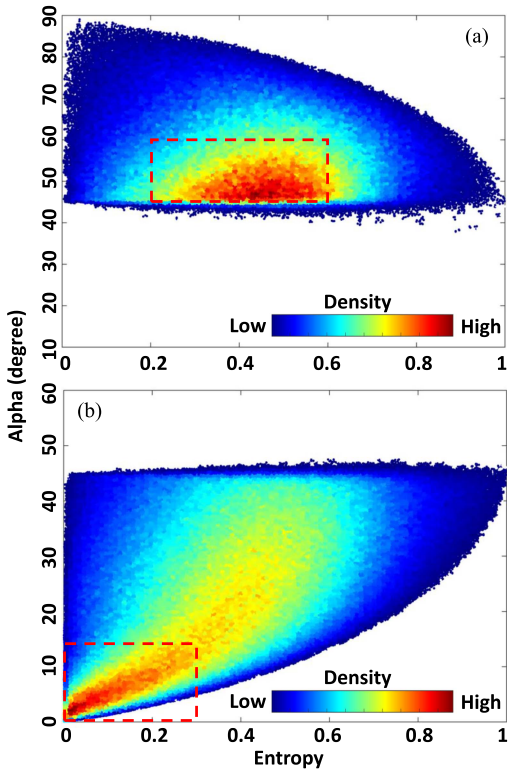

Fig. 13. H-Alpha scatter plot for the high quality pixels, i.e., pixels with ESM-TPC higher than 0.9. (a) for the pixels with $4 \cdot \overline{|S_{\mathrm{vh}}|}^2 > \overline{|S_{\mathrm{vv}}|}^2$, (b) for the other pixels with $4 \cdot \overline{|S_{\mathrm{vh}}|}^2 \leq \overline{|S_{\mathrm{vv}}|}^2$.

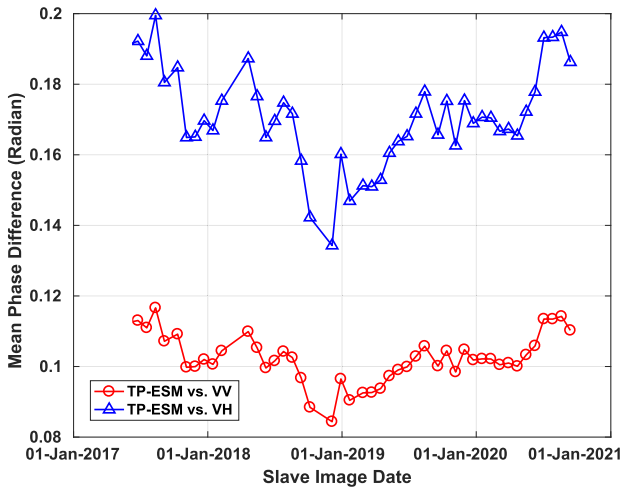

Fig. 14. IMPD values between interferogram pair (TP-ESM, VV) and (TP-ESM, VH). For the interferogram pair (TP-ESM, VV), only those TP-ESM selected pixels with VV channel weights bigger than that of VH are included in the IMPD calculation. On the other hand, only those TP-ESM selected pixels with VV channel weights smaller than that of VH are used to calculate the IMPD for the (TP-ESM, VH) pair. As the interferogram is generated with the single-master method, they can be represented by their slave image date as the X-axis shows.

Sentinel-1 data set in this study. However, with small modifications, it can be applied to other kinds of PolSAR images. Based on the previous analysis, it can be found that the performance of TP-ESM is mainly determined by the quality of PolSAR images' temporal mean amplitudes (under Pauli basis). With longer wavelength, higher resolution or full-polarization PolSAR images (like ALOS-2 or Radarsat-2 PolSAR images) the SMs of pixels could be better represented by their corresponding temporal mean amplitudes. Thus, the proposed TP-ESM algorithm is expected to have better performance on these PolSAR images than with DP Sentinel-1 data, as shown in this study.

Meanwhile, for the existing PolSAR images with shorter wavelength (f.i., X-band) but higher resolutions (like TerraSAR-X and Cosmo-Skymed-2 PolSAR images), better performances achieved by TP-ESM are also expected. This is because that the speckle noise that seriously affects the shorter wavelength SAR amplitude images can be mostly reduced by the temporal average of amplitudes, and better resolution would benefit the representation of the dominant SM in each resolution cell by the weights in TP-ESM [see (10)]. To conclude, the proposed TP-ESM algorithm is anticipated to have a better performance on the other existing PolSAR images than DP Sentinel-1 data.

E. Limitations of the Proposed TP-ESM

The main limitation of the proposed TP-ESM method is its performance on DS pixels' optimizations, although it outperforms the ESPO method. This is because TP-ESM does not apply any adaptive filtering on DS pixels with its polarimetric homogeneous pixels, which is usually time-consuming. As the result, its improvement on DS pixels' interferometric phase optimization and ground deformation monitoring is limited. One possible approach to overcome this limitation is to first apply the adaptive filtering on all pixels [45], [49] and then carry out the TP-ESM optimization. The other limitation of TP-ESM, which can be inferred from the abovementioned experiment results, is that its overall performance for PSI applications is not as good as ESPO. Thus, for the applications where intensive computation burden is acceptable and very detailed ground deformation monitoring results are desired, ESPO is better than TP-ESM.

VI. Conclusion

An efficient and effective PolPSI algorithm, i.e., TP-ESM, is proposed in this study for the DP Sentinel-1 data. To validate its effectiveness, together with the TP-MSM and ESPO methods, the proposed TP-ESM has been tested on the Sentinel-1 dataset over Beijing.

For the interferogram optimization, the proposed TP-ESM and ESPO are both able to improve pixels' interferometric phase qualities, and ESPO overall performs slightly better than the proposed TP-ESM over the test area. The interferogram optimization results of the proposed TP-ESM is determined by both VV and VH channel, where the VV channel in general plays a more important role. In addition, the proposed TP-ESM is found to have better DS pixels' optimization effect than ESPO with D_A optimization. On the contrary, the TP-MSM methods' performance is unstable and unsatisfactory on DP Sentinel-1 data, where it overall decreases pixels' interferometric phase qualities. Thus, as the results of this study indicate the TP-MSM method is not applicable on Sentinel-1 data for pixels' polarimetric optimizations.

For the ground deformation monitoring, the final pixel number obtained by the VV (i.e., the conventional PSI method), TP-MSM, TP-ESM, and ESPO approach is 1 740 206, 986 217, 2 356 268, and 2 492 681, respectively. Thus, the corresponding increase or decrease in pixel density achieved by the TP-MSM, TP-ESM, and ESPO w.r.t. the VV approach is -43%, 35%, and 43%, respectively. Except the TP-MSM method, more deformation details can be obtained by the proposed TP-ESM and ESPO than the VV approach.

The computation cost of the proposed TP-ESM is very small and negligible w.r.t. ESPO. The high efficiency and effectiveness of the proposed TP-ESM algorithm make it a promising PolPSI technique for the ground deformation monitoring over large regions with Sentinel-1 data. Moreover, TP-ESM is anticipated to have good or even better performances on the other kinds of PolSAR images than Sentinel-1 data, which is also the authors' further research focus.

Acknowledgment

The authors would like to thank European Space Agency (ESA) for providing Sentinel-1 data and the World-Cover 10 m 2020 product. The groundwater data were published by the Beijing Water Authority. Some figures were prepared using the public domain GMT software (Wessel and Smith, 1998). Optical images provided by GoogleEarth.

References

[1] D. Massonnet et al., "The displacement field of the landers earthquake mapped by radar interferometry," *Nature*, vol. 364, no. 6433, pp. 138–142, 1993.
[2] M. E. Pritchard and M. Simons, "A satellite geodetic survey of large-scale deformation of volcanic centres in the central andes," *Nature*, vol. 418, no. 6894, pp. 167–171, 2002.
[3] L. Gray, "Using multiple radarsat inSAR pairs to estimate a full three-dimensional solution for glacial ice movement," *Geophysical Res. Lett.*, vol. 38, no. 5, pp. 1–6, Mar. 2011.
[4] H. Zebker and J. Villasenor, "Decorrelation in interferometric radar echoes," *IEEE Trans. Geosci. Remote Sens.*, vol. 30, no. 5, pp. 950–959, Sep. 1992.
[5] R. F. Hanssen, *Radar Interferometry: Data Interpretation and Error Analysis*, vol. 2. Berlin, Germany: Springer, 2001.
[6] A. Ferretti, C. Prati, and F. Rocca, "Nonlinear subsidence rate estimation using permanent scatterers in differential SAR interferometry," *IEEE Trans. Geosci. Remote Sens.*, vol. 38, no. 5, pp. 2202–2212, Sep. 2000.
[7] A. Ferretti, C. Prati, and F. Rocca, "Permanent scatterers in SAR interferometry," *IEEE Trans. Geosci. Remote Sens.*, vol. 39, no. 1, pp. 8–20, Jan. 2001.
[8] P. Berardino, G. Fornaro, R. Lanari, and E. Sansosti, "A new algorithm for surface deformation monitoring based on small baseline differential SAR interferograms," *IEEE Trans. Geosci. Remote Sens.*, vol. 40, no. 11, pp. 2375–2383, Nov. 2002.
[9] O. Mora, J. J. Mallorqui, and A. Broquetas, "Linear and nonlinear terrain deformation maps from a reduced set of interferometric SAR images," *IEEE Trans. Geosci. Remote Sens.*, vol. 41, no. 10, pp. 2243–2253, Oct. 2003.
[10] R. Lanari, O. Mora, M. Manunta, J. J. Mallorquí, P. Berardino, and E. Sansosti, "A small-baseline approach for investigating deformations on full-resolution differential SAR interferograms," *IEEE Trans. Geosci. Remote Sens.*, vol. 42, no. 7, pp. 1377–1386, Jul. 2004.
[11] A. Hooper, H. Zebker, P. Segall, and B. Kampes, "A new method for measuring deformation on volcanoes and other natural terrains using InSAR persistent scatterers," *Geophysical Res. Lett.*, vol. 31, no. 23, pp. 1–5, Dec. 2004.
[12] A. Hooper, P. Segall, and H. Zebker, "Persistent scatterer interferometric synthetic aperture radar for crustal deformation analysis, with application to volcán alcedo, galápagos," *J. Geophysical Res.: Solid Earth*, vol. 112, no. B7, pp. 1–21, Jul. 2007.
[13] Z. Hu, J. J. Mallorqui, and H. Fan, "Atmospheric artifacts correction with a covariance-weighted linear model over mountainous regions," *IEEE Trans. Geosci. Remote Sens.*, vol. 56, no. 12, pp. 6995–7008, Dec. 2018.
[14] Z. Hu and J. J. Mallorquí, "An accurate method to correct atmospheric phase delay for inSAR with the era5 global atmospheric model," *Remote Sens.*, vol. 11, no. 17, 2019, Art. no. 1969.
[15] F. Zhao, Y. Wang, S. Yan, and L. Lin, "Reconstructing the vertical component of ground deformation from ascending also and descending envisat datasets—A case study in the Cangzhou area of China," *Can. J. Remote Sens.*, vol. 42, no. 3, pp. 147–160, 2016.
[16] F. Cigna and D. Tapete, "Present-day land subsidence rates, surface faulting hazard and risk in Mexico city with 2014–2020 sentinel-1 IW inSAR;," *Remote Sens. Environ.*, vol. 253, 2021, Art. no. 112161.
[17] S. Du, J. J. Mallorqui, H. Fan, and M. Zheng, "Improving PSI processing of mining induced large deformations with external models," *Remote Sens.*, vol. 12, no. 19, 2020, Art. no. 3145.
[18] F. Liu, J. Elliott, T. Craig, A. Hooper, and T. Wright, "Improving the resolving power of inSAR for earthquakes using time series: A case study in Iran," *Geophysical Res. Lett.*, vol. 48, no. 14, 2021, Art. no. e2021GL093043.
[19] J. Fernández et al., "Detection of volcanic unrest onset in La Palma, Canary islands, evolution and implications," *Sci. Rep.*, vol. 11, no. 1, pp. 1–15, 2021.

[20] F. Zhao, J. J. Mallorqui, R. Iglesias, J. Gili, and J. Corominas, "Landslide monitoring using multi-temporal SAR interferometry with advanced persistent scatterers identification methods and super high-spatial resolution TerraSAR-X images," *Remote Sens.*, vol. 10, no. 6, pp. 1–23, Jun. 2018.

[21] J. Liu et al., "Underground coal fire detection and monitoring based on landsat-8 and sentinel-1 data sets in miquan fire area, Xinjiang," *Remote Sens.*, vol. 13, no. 6, 2021, Art. no. 1141.

[22] A. Ferretti, A. Fumagalli, F. Novali, C. Prati, F. Rocca, and A. Rucci, "A new algorithm for processing interferometric data-stacks: SqueeSAR," *IEEE Trans. Geosci. Remote Sens.*, vol. 49, no. 9, pp. 3460–3470, Sep. 2011.

[23] Y. Du, S. Yan, F. Zhao, D. Chen, and H. Zhang, "DS-inSAR based long-term deformation pattern analysis in the mining region with an improved phase optimization algorithm," *Front. Environ. Sci.*, vol. 10, p. 55, 2022.

[24] G. Fornaro, S. Verde, D. Reale, and A. Pauciullo, "CAESAR: An approach based on covariance matrix decomposition to improve multibaseline–multitemporal interferometric SAR processing," *IEEE Trans. Geosci. Remote Sens.*, vol. 53, no. 4, pp. 2050–2065, Apr. 2015.

[25] Y. Wang, X. Zhu, and R. Bamler, "Retrieval of phase history parameters from distributed scatterers in urban areas using very high resolution SAR data," *ISPRS J. Photogrammetry Remote Sens.*, vol. 73, pp. 89–99, 2012.

[26] N. Cao, H. Lee, and H. C. Jung, "A phase-decomposition-based PSInSAR processing method," *IEEE Trans. Geosci. Remote Sens.*, vol. 54, no. 2, pp. 1074–1090, Feb. 2016.

[27] M. Jiang, X. Ding, R. F. Hanssen, R. Malhotra, and L. Chang, "Fast statistically homogeneous pixel selection for covariance matrix estimation for multitemporal InSAR," *IEEE Trans. Geosci. Remote Sens.*, vol. 53, no. 3, pp. 1213–1224, Mar. 2015.

[28] A. M. Guarnieri and S. Tebaldini, "On the exploitation of target statistics for SAR interferometry applications," *IEEE Trans. Geosci. Remote Sens.*, vol. 46, no. 11, pp. 3436–3443, Nov. 2008.

[29] H. Ansari, F. De Zan, and R. Bamler, "Efficient phase estimation for interferogram stacks," *IEEE Trans. Geosci. Remote Sens.*, vol. 56, no. 7, pp. 4109–4125, Jul. 2018.

[30] M. Jiang and A. M. Guarnieri, "Distributed scatterer interferometry with the refinement of spatiotemporal coherence," *IEEE Trans. Geosci. Remote Sens.*, vol. 58, no. 6, pp. 3977–3987, Jun. 2020.

[31] C. Wang et al., "A new likelihood function for consistent phase series estimation in distributed scatterer interferometry," *IEEE Trans. Geosci. Remote Sens.*, vol. 60, no. 4, Apr. 2022, Art. no. 5227314.

[32] J. Eppler and B. T. Rabus, "Adapting inSAR phase linking for seasonally snow-covered terrain," *IEEE Trans. Geosci. Remote Sens.*, vol. 60, no. 6, Jun. 2022, Art. no. 4305313.

[33] S. R. Cloude and K. P. Papathanassiou, "Polarimetric SAR interferometry," *IEEE Trans. Geosci. Remote Sens.*, vol. 36, no. 5, pp. 1551–1565, Sep. 1998.

[34] J.-S. Lee and E. Pottier, *Polarimetric Radar Imaging: From Basics to Applications*. Boca Raton, FL, USA: CRC Press, 2009.

[35] L. Pipia et al., "Polarimetric differential SAR interferometry: First results with ground-based measurements," *IEEE Geosci. Remote Sens. Lett.*, vol. 6, no. 1, pp. 167–171, Jan. 2009.

[36] V. D. Navarro-Sanchez, J. M. Lopez-Sanchez, and F. Vicente-Guijalba, "A contribution of polarimetry to satellite differential SAR interferometry: Increasing the number of pixel candidates," *IEEE Geosci. Remote Sens. Lett.*, vol. 7, no. 2, pp. 276–280, Apr. 2010.

[37] V. D. Navarro-Sanchez and J. M. Lopez-Sanchez, "Improvement of persistent-scatterer interferometry performance by means of a polarimetric optimization," *IEEE Geosci. Remote Sens. Lett.*, vol. 9, no. 4, pp. 609–613, Apr. 2012.

[38] V. D. Navarro-Sanchez, J. M. Lopez-Sanchez, and L. Ferro-Famil, "Polarimetric approaches for persistent scatterers interferometry," *IEEE Trans. Geosci. Remote Sens.*, vol. 52, no. 3, pp. 1667–1676, Mar. 2014.

[39] V. D. Navarro-Sanchez and J. M. Lopez-Sanchez, "Spatial adaptive speckle filtering driven by temporal polarimetric statistics and its application to PSI," *IEEE Trans. Geosci. Remote Sens.*, vol. 52, no. 8, pp. 4548–4557, Aug. 2014.

[40] R. Iglesias, D. Monells, X. Fabregas, J. J. Mallorqui, A. Aguasca, and C. Lopez-Martínez, "Phase quality optimization techniques and limitations in polarimetric differential SAR interferometry," *Transformation*, vol. 17, pp. 1–8, Jan. 2013.

[41] R. Iglesias, D. Monells, X. Fabregas, J. J. Mallorqui, A. Aguasca, and C. Lopez-Martinez, "Phase quality optimization in polarimetric differential SAR interferometry," *IEEE Trans. Geosci. remote Sens.*, vol. 52, no. 5, pp. 2875–2888, May 2014.

[42] M. Esmaeili and M. Motagh, "Improved persistent scatterer analysis using amplitude dispersion index optimization of dual polarimetry data," *ISPRS J. Photogrammetry Remote Sens.*, vol. 117, pp. 108–114, 2016.

[43] A. G. Mullissa, D. Perissin, V. A. Tolpekin, and A. Stein, "Polarimetry-based distributed scatterer processing method for PSI applications," *IEEE Trans. Geosci. Remote Sens.*, vol. 56, no. 6, pp. 3371–3382, Jun. 2018.

[44] Z. Sadeghi, M. J. V. Zoej, A. Hooper, and J. M. Lopez-Sanchez, "A new polarimetric persistent scatterer interferometry method using temporal coherence optimization," *IEEE Trans. Geosci. Remote Sens.*, vol. 56, no. 11, pp. 6547–6555, Nov. 2018.

[45] F. Zhao and J. J. Mallorqui, "SMF-POLOPT: An adaptive multitemporal Pol(DIn)SAR filtering and phase optimization algorithm for PSI applications," *IEEE Trans. Geosci. Remote Sens.*, vol. 57, no. 9, pp. 7135–7147, Sep. 2019.

[46] F. Zhao and J. J. Mallorqui, "Coherency matrix decomposition-based polarimetric persistent scatterer interferometry," *IEEE Trans. Geosci. Remote Sens.*, vol. 57, no. 10, pp. 7819–7831, Oct. 2019.

[47] G. Wang et al., "A phase optimization method for DS-inSAR based on SKP decomposition from quad-polarized data," *IEEE Geosci. Remote Sens. Lett.*, vol. 19, no. 1, Jan. 2021, Art. no. 4008805.

[48] P. Shen et al., "A novel polarimetric PSI method using trace moment-based statistical properties and total power interferogram construction," *IEEE Trans. Geosci. Remote Sens.*, vol. 60, no. 7, Jul. 2021, Art. no. 4402815.

[49] F. Zhao et al., "Polarimetric persistent scatterer interferometry for ground deformation monitoring with VV-VH sentinel-1 data," *Remote Sens.*, vol. 14, no. 2, pp. 1–26, Jan. 2022.

[50] R. Iglesias, D. Monells, C. López-Martínez, J. J. Mallorqui, X. Fabregas, and A. Aguasca, "Polarimetric optimization of temporal sublook coherence for DInSAR applications," *IEEE Geosci. Remote Sens. Lett.*, vol. 12, no. 1, pp. 87–91, Jan. 2015.

[51] F. Zhao, J. J. Mallorqui, and J. M. Lopez-Sanchez, "Impact of SAR image resolution on polarimetric persistent scatterer interferometry with amplitude dispersion optimization," *IEEE Trans. Geosci. Remote Sens.*, vol. 60, Feb. 2022, Art. no. 5202810.

[52] R. Shamshiri, H. Nahavandchi, and M. Motagh, "Persistent scatterer analysis using dual-polarization sentinel-1 data: Contribution from VH channel," *IEEE J. Sel. Topics Appl. Earth Observ. Remote Sens.*, vol. 11, no. 9, pp. 3105–3112, Sep. 2018.

[53] S. Azadnejad, Y. Maghsoudi, and D. Perissin, "Evaluation of polarimetric capabilities of dual polarized sentinel-1 and terrasar-X data to improve the PSinSAR algorithm using amplitude dispersion index optimization," *Int. J. Appl. Earth Observ. Geoinformation*, vol. 84, 2020, Art. no. 101950.

[54] M. Neumann, L. Ferro-Famil, and A. Reigber, "Multibaseline polarimetric SAR interferometry coherence optimization," *IEEE Geosci. Remote Sens. Lett.*, vol. 5, no. 1, pp. 93–97, Jan. 2008.

[55] F. Zhao and J. J. Mallorqui, "A temporal phase coherence estimation algorithm and its application on DInSAR pixel selection," *IEEE Trans. Geosci. Remote Sens.*, vol. 57, no. 11, pp. 8350–8361, Nov. 2019.

[56] B. Chen et al., "Land subsidence and its relation with groundwater aquifers in Beijing plain of China," *Sci. Total Environ.*, vol. 735, 2020, Art. no. 139111.

[57] K. Lei et al., "Three-dimensional surface deformation characteristics based on time series inSAR and GPS technologies in Beijing, China," *Remote Sens.*, vol. 13, no. 19, 2021, Art. no. 3964.

[58] Z. Du et al., "Analysis of the impact of the south-to-north water diversion project on water balance and land subsidence in Beijing, China between 2007 and 2020," *J. Hydrol.*, vol. 603, 2021, Art. no. 126990.

[59] Y. Li, H. Gong, L. Zhu, and X. Li, "Measuring spatiotemporal features of land subsidence, groundwater drawdown, and compressible layer thickness in Beijing plain, China," *Water*, vol. 9, no. 1, pp. 1–17, Feb. 2017.

[60] S. R. Cloude and E. Pottier, "An entropy based classification scheme for land applications of polarimetric SAR," *IEEE Trans. Geosci. Remote Sens.*, vol. 35, no. 1, pp. 68–78, Jan. 1997.

[61] M. Chini, R. Pelich, R. Hostache, P. Matgen, and C. Lopez-Martinez, "Polarimetric and multitemporal information extracted from sentinel-1 SAR data to map buildings," in *Proc. IEEE Int. Geosci. Remote Sens. Symp.*, 2018, pp. 8132–8134.

[62] A. Verma, S. Dey, N. Bhogapurapu, C. López-Martínez, and A. Bhattacharya, "Dual polarimetric SAR signature for human-made target characterization," in *Proc. IEEE Int. India Geosci. Remote Sens. Symp.*, 2021, pp. 520–523.

[63] L. Pulvirenti, M. Chini, N. Pierdicca, and G. Boni, "Use of SAR data for detecting floodwater in urban and agricultural areas: The role of the interferometric coherence," *IEEE Trans. Geosci. Remote Sens.*, vol. 54, no. 3, pp. 1532–1544, Mar. 2016.

Feng Zhao (Member, IEEE) received the M.S. degree in geodesy and survey engineering from the China University of Mining and Technology (CUMT), Xuzhou, China, in June 2016 and the Ph.D. degree in signal theory and communications from the Universitat Politècnica de Catalunya, Barcelona, Spain, in September 2019.

Since November 2019, he has been with the School of Environment Science and Spatial Informatics, CUMT, and with the Jiangsu Key Laboratory of Resources and Environmental Information Engineering, CUMT, first as an Assistant Professor, and since 2023 as an Associate Professor. His main work focuses on the development of advanced pixel selection and optimization algorithms for multitemporal (Pol)InSAR techniques. His research interests include advanced multitemporal InSAR techniques and their application in terrain deformation detection and disaster monitoring.

Leixin Zhang received the B.S. degree in surveying and mapping engineering from the China University of Mining and Technology, Beijing, China, in 2020. He is currently working toward the Ph.D. degree in geodesy and surveying engineering with the China University of Mining and Technology, Xuzhou, China.

His current research interests include coal fire monitoring, interferometric synthetic aperture radar data processing, and deformation monitoring.

Teng Wang received the B.S. degree in surveying and mapping engineering in 2020 from the China University of Mining and Technology, Xuzhou, China, where he is currently working toward the Ph.D. degree in geodesy and surveying engineering.

His current research interests include coal fire monitoring, interferometric synthetic aperture radar data processing, and deformation monitoring.

Yuxuan Zhang received the B.S. degree in surveying and mapping engineering in 2021 from the China University of Mining and Technology, Xuzhou, China, where she is currently working toward the M.A. degree in geodesy and surveying engineering.

Her current research interests include coal fire monitoring, interferometric synthetic aperture radar data processing, and deformation monitoring.

Shiyong Yan received the Ph.D. degree in cartography and geographic information systems from the Institute of Remote Sensing and Digital Earth, Chinese Academy of Sciences, Beijing, China, in 2013.

He is currently an Associate Professor with the China University of Mining and Technology. His research interests include InSAR technology and application, remote sensing image processing, and remote sensing disaster monitoring and evaluation.

Yunjia Wang received the M.Eng. degree in mine surveying and the Ph.D. degree in mining engineering from the China University of Mining and Technology, Xuzhou, China, in 1988 and 2000, respectively.

From 2002 to 2004, he was a Postdoctoral Fellow with the China University of Mining and Technology. He joined the Royal Melbourne Institute of Technology, Melbourne, VIC, Australia, as a Visiting Research Scholar, in 2006, and the Ryerson University, Toronto, ON, Canada, in 2014. He is currently a Full Professor with the School of Environmental Science and Spatial Informatics, China University of Mining and Technology. His research interests include ubiquitous positioning and navigation, disaster monitoring, and coal fire monitoring.